DOI: 10.15480/882.9326

Eighth International Symposium on Marine Propulsors
smp'24, Berlin, Germany, March 2024

Underwater Radiated Noise of a Double Ended Ferry with SRE Thrusters

Julian Kimmerl[1], Andreas Bender[1], Eric Steffens[1], Raphael Bevand[2], Robert Beckmann[2], Moustafa Abdel-Maksoud[2]

[1]SCHOTTEL GmbH, Dörth, Germany
[2]Institute for Fluid Dynamics and Ship Theory, Hamburg University of Technology (TUHH), Hamburg, Germany

ABSTRACT

Regulations regarding underwater radiated noise of marine vessels are expected to become more strict in the near future as a result of updated international guidelines. For a ferry with a Schottel EcoPeller (SRE) type thruster unit, an investigation campaign consisting of a underwater noise measurement and several simulation types is conducted. The hydrodynamic flow is investigated with several simulation approaches under consideration of cavitation effects and the interaction between the vessel and the propulsion unit. A unidirectional coupling between the hydrodynamic loads and the thruster structure is established to evaluate the complete acoustic emissions of the propulsor considering structural contributions and is compared on a spherical control surface around the unit. For the far-field, single noise observers are evaluated by applying an acoustic analogy. From the investigation results, the contributions of the propeller hydrodynamic, propulsion unit mechanical and vessel machinery noise are identified. Moderate agreement of the sound pressure level between measurement and simulations is achieved depending on frequency, with the largest unconsidered contribution originating from vessel machinery. In conclusion, the complete acoustic signature of the vessel and propulsion unit for the investigated operation point complies with classification societies limits in both measurement and simulations.

Keywords

Azimuthing Thruster, CFD, Full-scale Measurement, URN

1 INTRODUCTION

The revised underwater radiated noise (URN) guidelines from July 2023 (IMO 2023) extend far beyond the previous revision of 2014 by denoting clear goals to reduce anthropogenic noise as a result of global shipping by incentivizing the implementation of restriction zones in waters of particular relevance to marine life. This is prepared by classification societies such as BV and DNV by releasing their own URN class notations. While research activities concerning the impact of noise on marine biological species e.g. including frequency, season, region and their severity on the organism are still at an early stage, the state of ship building engineering is now sufficiently developed to evaluate URN over large ranges of frequencies. As a result, designers, shipyards and operators require knowledge about the underwater signatures of their vessels depending on the respective operation point. To alleviate the risk imposed by sea trial measurements without prior sufficient knowledge of acoustic emissions of components, suppliers are asked to provide predictions about the noise emissions such as the propulsion units beforehand. To acquire the full URN signature on the one hand and the excitation of the hull on the other for an azimuthing propulsion unit, the single components result in a complex noise signal composed of the hydrodynamic noise of the propeller and the vibrating unit as well as the structural reaction to the periodic excitation, the propeller cavitation noise, the gear mesh frequency, bearing noise and possibly an electric engine powering a compact unit.

The progress of high-fidelity hydrodynamic simulations of URN has been advancing rapidly over the last decade for both finite volume based geometric discretization methods (FVM) as well as panel based boundary element methods (BEM). A benchmark for the validation of the computation of URN emissions induced by propellers under open water conditions using the FVM is established, for example, for the Newcastle Propeller Test Case (Kimmerl et al. 2021) (Sezen et al. 2021), while the prediction for conventional propeller hull configurations is maturing to a similar status as proven for example by a BEM investigation of a catamaran (Göttsche et al. 2019) or a propeller-hull configurations with rudder (Krasilnikov et al. 2022). For tackling the acoustic emissions in combination with the

hydrodynamic simulations the permeable surface Ffowcs-Williams Hawkings (FWH) method is introduced (Lidtke et al. 2016) and now commonly utilized. It is validated for simple test cases and was recently applied to propeller-hull configurations with rudder. (Kimmerl et al. 2022) On the mechanical simulation side, publications of research regarding URN are surprisingly sparse, however, it is known that software simulation providers have solutions available to obtain first approximations with finite element methods (FEM).

Full-scale measurements of URN are well established and standardized (ITTC 2017), however, depend highly on environmental conditions and proper precautions to exclude signal noise, which is difficult to ensure in practice. While there are standardized test tracks reaching exceptional reproducibility, many hydroacoustic measurements are conducted with handheld hydrophones or buoy mounted devices.

In this study, an azimuthing thruster is investigated in full-scale regarding the complete URN emissions, by taking a measurement with an available unit in a ferry that is optimized for efficiency at the design point and comparing it with simulation results from BEM, FVM and coupled FEM.

2 TEST CASE

The double ended car ferry in Figure 1 (a) with a Schottel SRE 560 type propulsion unit at each end on the center line is investigated. The unit is a controllable pitch azimuthing propulsor in pull-configuration with a tailfin. The thruster is installed with an inclination of 3° downwards towards the ship center. The efficiency optimized propeller listed with the main parameters in Table 1 stems from a design for fast transit at $v_s = 19.8kn$ with a given power. The draft during the measurement is $T = 4.5m$, with the vessel fully bunkered, but without any cargo or passengers, which is equivalent to ballast draft. The trim during the measurement run is negligible with $\varphi = -0.03°$ and is thus not considered in the simulations. The coordinate origin for the simulation work is at the intersection of the propeller shaftline with the vertical shaftline of the unit with the z-axis pointing against the gravitation vector, which is also considered as the center of the noise emission or for determining the closest point of approach (CPA) to the measurement hydrophone in the URN measurements.

(a) Photography at port arrival

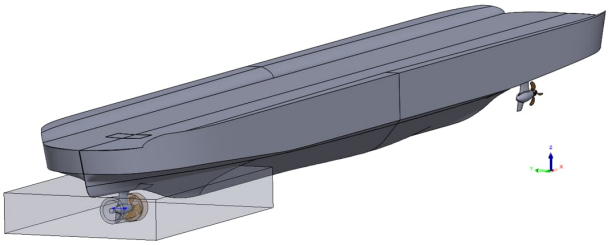

(b) Hydrodynamic simulation model with refinements

Figure 1: Test Case

To isolate the unit noise, an artificial test condition is constructed with only the aft thruster operating at the operation point in Table 2, which results in the propeller operating close to the design condition, and the front unit in full-feathering condition to minimize its interference of the aft propulsor wake and noise emissions as shown in Figure 1 (b). All values in the table are collected from the controller area network signal on the vessel and averaged over the URN measurement time, although variation in steering angle, input speed and pitch are negligible.

The unit is powered by a vertically mounted electric drive motor integrated into the baseplate with a noise emission between $100Hz < f < 600Hz$ and two significant peaks at $f = 232Hz$ and $f = 464Hz$. Generator sets on the vessel are running during the measurement, with their noise generation unknown. The clock frequency inverter creates a peak at $f = 2896Hz$.

Table 1: Propeller main parameters

Diameter	Pitch r/R = 0.7	Area Ratio	Skew	Number of Blades
[m]	[-]	[-]	[°]	[-]
3.1	1.052	0.486	29.4	4

Table 2: Mean values during investigated run

Azimuth	Input Speed	Pitch r/R = 0.7	Power	Vessel Speed
[°]	[rpm]	[°]	[%]	[kn]
180.8	169.5	27.52	-9.1%	14.4

The resulting wave pattern at the given operation point from a Reynolds-averaged Navier-Stokes (RANS) equation based two phase resistance simulation is shown in Figure 2, which is used as a static top domain boundary for the FVM simulation, while the BEM considers a flat surface for the acoustic emission. The FEM simulation does not consider the surrounding medium, as the simulation domain ends at the interface of the underwater housing with the water. The acoustic methods for the FEM and FVM also neglect the reflections at the water surface and the sea floor, while the BEM is able to separately include the contributions.

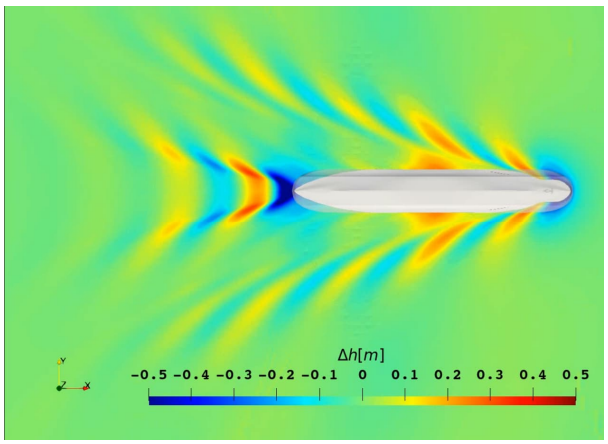

Figure 2: Test case wave pattern, RANS CFD

3 METHODS

The methods involved in this study are the computational fluid dynamics (CFD) methods BEM and FVM, the structural simulations with FEM and experimental measurements. All simulations are full-scale.

3.1 CFD

3.1.1 Panel Method

The BEM panel method is a time domain approach where the velocity field $\vec{u}\,(\vec{x},t)$ is computed from the gradient of an unsteady velocity potential $\Phi(\vec{x},t)$. The flow model is derived by neglecting viscosity and compressiblity in the Navier-Stokes equations. This results in the Laplace equation $\Delta\Phi = 0$ for the mass conservation and the Bernoulli equation

$$\frac{p}{\rho} + g \cdot \vec{x} + \frac{1}{2}\nabla\Phi \cdot \nabla\Phi + \frac{\partial\Phi}{\partial t} = const. \qquad (1)$$

for the momentum conservation. By applying Green's second identity, the Laplace equation can be transformed from a volume to a surface integral over the surfaces bounding the fluid volume. The potential distribution on the bounding surface is determined by kinematic and dynamic boundary conditions. Due to the linearity of the Laplace equation, the potential can be expressed as a superposition of different potential solutions. In the following study, the panel method panMARE (FDS-TUHH 2023) is applied to calculate the propeller flow and the pressure field in the fluid domain. It is based on the formulation by Smith and Hess (Katz & Plotkin 2001). The smooth surfaces are numerically discretized into panels, see Figure 3. On each panel a constant source strength and doublet strength potential are distributed, which locally induce radial and vortex flows, respectively. The total velocity potential is given by $\Phi = \Phi_I + \Phi_E - \Phi_M$, with the motion potential Φ_M, the induced potential Φ_I and the external potential Φ_E. At the sharp trailing edge of the propeller blades, the Kutta condition is applied to model the free shear sheet. The so called wake panels transport the doublet strength difference between suction and pressure side body panels downstream. Doublet strength differences between adjacent free shear sheet panels lead to its characteristic roll-up motion. The inhomogeneous inflow velocity field (ship wake) in front of the propeller, which results from viscosity effects on the ship hull, is applied as an external potential. The gondola and the propeller shaft are not discretized, as the interaction between the free shear sheet (green surface) and the gondola (white surface) lead to numerical issues in the current implementation due to the induced potential singularity at panel edges. The inhomogeneous inflow velocity field or ship wake in front of the propeller, which results from viscosity effects on the ship hull, has to be applied indirectly as an external potential. The corresponding external potential velocity field is shown in Figure 3 right of the propeller. During the simulation, it is superposed with the ship motion velocity in order to reproduce the inflow velocity field.

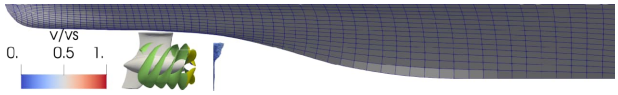

Figure 3: Discretized surfaces of propeller, free shear sheet and ship hull

After the velocity field is computed for a given time step, a second iteration is applied to determine the partial sheet cavity extent due to the actual pressure distribution. The numerical model is based on the work from Kinnas et al. (2003) and its implementation is described in Gaschler (2017). The cavity thickness varies over time, contributing considerably to the acoustic pressure field. Only sheet cavitation is considered. Thus, only contributions up to $150Hz$ can be estimated in the acoustic spectrum. Contributions from e.g. the tip vortex are therefore neglected.

During the simulation, the unsteady pressure field and the potential solution on each panel is stored. Afterwards, in a post-processing step this data is used to integrate the Ffowcs-Williams Hawkings equations in their Farassat 1A formulation (Farassat 1981). The sound path is divided into a direct path from the panels as well as the reflections at the free surface and the seafloor (Göttsche 2020).

3.1.2 Finite Volume Method

The finite volume method solves a time domain incompressible, adiabatic, pressure based system with two immiscible phases water and water vapor modeled as an homogeneous Euler mixture with the volume of fluid method and an active phase transition based on the Schnerr-Sauer cavitation model with the model coefficients $n_0 = 1 \cdot 10^{12} 1/m^3$ and $d_{nuc} = 1 \cdot 10^{-4} m$. A cylindrical sliding mesh around the propeller axis is used to model the dynamic propeller rotation in the simulation.

A full geometric model for the propeller geometry is simulated with the OpenFOAM solver *interPhaseChangeDyMFoam* distributed as Engys HELYX-core version 3.5.1 with the governing equations

$$\frac{\partial \rho_m}{\partial t} + \frac{\partial(\rho_m u_i)}{\partial x_i}, \qquad (2)$$

$$\frac{\partial(\rho_m u_i)}{\partial t} + \frac{\partial(\rho_m u_i u_j)}{\partial x_j} = \frac{\partial}{\partial x_j}\left(\mu\left(\frac{\partial u_i}{\partial x_j} + \frac{\partial u_j}{\partial x_i}\right)\right) - \frac{\partial p}{\partial x_j} + \rho_m g, \quad (3)$$

with the mixture density ρ_m. Turbulence is modelled initially by RANS with k - ω -SST by introducing a turbulent eddy viscosity μ_t and subsequently by implicit Large Eddy Simulation (LES) with wall modelling and a mean CFL number below 1, while time discretization is first order for stability reasons. All shown evaluations of forces, flow field and noise are from the LES part. Regarding the boundary conditions, at the inlet the velocity is given according to the ship's speed as shown in Table 2 and at the outlet, the pressure is defined at the z-position of the origin. The deformation of the water surface is taken into account as a fixed geometry. The shape of the free surface is derived from an earlier simulation of the ship's flow without the propulsor but with the free water surface. The domain features an extent of $-41 \cdot D_p < x < 53 \cdot D_p$ and $-71 \cdot D_p < y < 71 \cdot D_p$with a depth of $z = 31 \cdot D_P$. Towards the boundaries of the domain the mesh is coarsening to dissipate pressure and possible pressure reflections. For complex geometries such as the propulsor-hull configuration the fitting of at least 10 layers on all solid surfaces for resolving the near wall flow determines the overall cell count. The cell dimensions of the mesh near the solid boundaries are reduced to the layer addition, while the number of cells is kept to a minimum except in highly relevant regions such as the aft of the vessel to accurately determine the flow around the thruster or the tip vortex region downstream of the propeller as indicated in Figure 1 (b).

For the computations of the far field acoustics, the Kirchhoff Ffowcs-Williams-Hawkings (KFWH) acoustic analogy (Francescantonio 1997) is evaluated for single point observers and the time domain results are transformed by FFT with a Hanning window with energy correction factor over 5 rotations. It consists of the first two pseudo-thickness and the following three pseudo-loading terms

$$p'(x,t) = \frac{1}{4\pi}\int_S \left[\frac{\rho_0(\dot{v}_n + v_{\dot{n}})}{r(1-M_r)^2}\right]_{ret} dS + \frac{1}{4\pi}\int_S \left[\frac{\rho_0 v_n (r\dot{M}_r + cM_r - cM^2)}{r^2|1-M_r|^3}\right]_{ret} dS + \frac{1}{4\pi c}\int_S \left[\frac{l_r}{r(1-M_r)^2}\right]_{ret} dS + \frac{1}{4\pi}\int_S \left[\frac{l_r - l_M}{r^2(1-M_r)^2}\right]_{ret} dS + \frac{1}{4\pi c}\int_S \left[\frac{l_r(r\dot{M}_r + cM_r - cM^2)}{r^2|1-M_r|^3}\right]_{ret} dS, \quad (4)$$

with the permeable passive surface S around the noise sources, the vectorial Mach number M, the surface normal velocity v_n and the distance between observer and source r, which is accounted for by the retarded time evaluation indicated by the bracket subscript ret. For the incompressible hull pressure pulses an averaging between adjacent frequencies leads to more accurate harmonics.

3.2 Structural

All structural investigations are conducted using Altair MotionView with the solver MotionSolve for multi body simulations (MBS), as well as the software HyperWorks with the solver OptiStruct for finite elements method (FEM) simulations.

3.2.1 MBS

To investigate the dynamics of the thruster, a MBS is carried out. The focus of the analyses is on determining the time-variant loads of the gearbox superimposed with the hydrodynamic loads. The bodies are modelled both rigidly and flexible by modal-reduced substitute systems. Rigidly modelled are bodies like propeller, electrical motor and the tooth of the bevel gear. The structure, shafts and the housing of the gearbox are modelled as flexible bodies. Flex bodies are modal-reduced by applying the Craig-Bampton method. The eigenvalues are calculated up to $3kHz$. The kinematics between the components are defined by joint-, bushing- and contact- elements. The meshing of the bevel gear is represented by a 3D mesh contact as a volume force model. This allows to derive the contact stiffness from physical material properties of the colliding bodies (pinion and crown wheel). The elastic spring force component of the normal force is calculated as

$$F_{spring} = A_{con} K z^{exp} \quad (5)$$

and the damping force as

$$F_{damping} = -c\frac{dz}{dt}, \quad (6)$$

with the contact penetration z, the exponent for the force deformation characteristic exp, the damping coefficient c and the area of the contact A_{con}. The contact stiffness K is calculated assuming that the springs for body i and j are in series.

$$K = \frac{\frac{M_i M_j}{d_i d_j}}{\frac{M_i}{d_i} + \frac{M_j}{d_j}}. \quad (7)$$

with the elastic modulus M and the layer depth d (Altair Engineering Inc. 2021).

Results of the MBS are dynamic bearing reaction loads. These loads are transformed from time domain to frequency domain and are used as complex input loads with amplitude, phase angle and frequency for the FEM acoustic simulation.

3.2.2 FEM

To calculate the response of the structure, a Frequency Response Analysis is conducted, using the Modal Superposition solution. The eigenvalue problem is solved using the Lanczos method. The harmonic excitation, caused by the bearing loads calculated by a MBS, is applied at the bearing location.

For the far field acoustics, the radiated sound method is used. This method measures the radiated sound generated by vibrating nodes, assuming the nodes to be discrete acoustic sources. It does not require any acoustic mesh

around the structure. The pressure at the microphone location for each frequency is calculated as

$$p = \sum_{j=1}^{np}\left(\frac{f\rho q}{r_j}\left(v_{flux}\right)_j i e^{-ikr_j}\right), \quad (8)$$

with the frequency of the sound wave in the medium f, the density of the acoustic medium ρ, the value of the scale factor q and the distance from the source grid j to the microphone location grid r_j. In addition, the number of source grids np and the velocity flux of the source grid v_{flux} as defined by

$$v_{flux} = v_s A \hat{A}_s, \quad (9)$$

is implemented with the velocity vector of the source grid v_s, the area associated with the source grid A and the unit area vector normal to the panel surface at the source grid $\hat{A}_s$. The wave number k is defined as

$$k = \frac{2\pi f}{c}, \quad (10)$$

with the speed of sound c (Altair Engineering Inc. 2021).

Another method, the Equivalent Radiated Power (ERP) method, is used to analyze and examine the structural noise. The ERP of a grid point is calculated as

$$ERP = \frac{1}{2} * R_{LF} c\rho \sum_{j=1}^{np}\left(A_j v_j^2\right), \quad (11)$$

with radiation loss factor R_{LF}, surface area of each element A_j and the normal velocity of each element v_j (Holm & Schubert 2021). Please note that the radiated acoustic power by the classic ERP tends to higher values at lower frequencies (Huang & Cui 2020). In this paper it is used to understand more about the mechanical radiation of noise and responsible areas.

3.3 Experimental

An underwater radiated noise measurement is performed on the car ferry where a stationary hydrophone is operated from a support boat that is passed by the vessel at dedicated out of operation light draft runs at a selected quiet measurement site. The support boat is completely shut down during the measurements to avoid contamination of the signal. Records are taken between 03:00h and 05:00h local time in the Bjornafjord in Norway. The water depth is $485m$ at calm sea condition. During the measurements, care was taken to ensure that no other ships were in the measurement area. A Reson TC4042 hydrophone is lowered to a depth of about 70 m. The received pressure signal is amplified by a Reson EC6073 and recorded with a Rion DA-21 datalogger at a sample rate of f_s = $51.2\ kHz$.

During the measurement the positions of both vessel and support boat are recorded. The received level is transformed to the source level by the implementation of ISO 17208-2:2019(E), A.3 (ISO/TC 43/SC 3 Underwater acoustics, 2019) in Weisang FlexPro 2021. For the final URN signature a measurement interval according to DNV SILENT class is considered, i.e. from abeam the front of the vessel until the transom of the vessel has passed the hydrophone by one ship length.

4 COMPARISON

In this section the different metrics of integral forces, flow field and noise evaluation are presented and where applicable compared between full-scale simulation results.

4.1 Thrust and Power

Comparing the resulting thrust and power to the prediction of a common in-house propulsion prognosis tool at design draft resistance ($T = 5.0m$) yields following results for the different approaches. The power signal over the measurement duration obtained from the vessel system fluctuates strongly, but it is higher than the expected power at the propulsor with 4.8% to 7.5%. As the measured power signal is the generator power, an estimation of the propeller power with considering hotel load, inverter and electric engine efficiency would be around -9.1%. In the BEM computation an averaged power of -12.1% is predicted at the propeller and the FVM propeller power during the acoustic evaluation yields an average of -14.1% compared to the expected power from the propulsion prognosis.

4.2 Flow Field

The resulting sheet cavitation from the BEM is illustrated in Figure 4, with significant portion of the suction side chord length cavitating beginning at the leading edge at the 12o'clock position and slight leading edge cavitation at the upwards going blade at 9o'clock.

A snapshot of the resulting flow field from FVM is given in Figure 5, with the Q-criterion and the vapor interface. Only with LES turbulence modelling the tip vortex reaches well beyond the unit, creating a vortical structure interaction that is leading to an additional excitation for the thruster structure and additional noise emitted onto the hull. The tested condition only shows a minor extent of leading edge suction side sheet cavitation between 3o'clock and 9o'clock with a peak at 12o'clock.

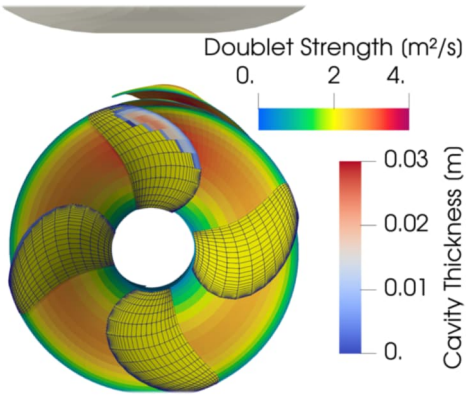

Figure 4: BEM propeller grid with estimated sheet cavity thickness and doublet strength on the free shear sheet

A possible explanation could be a small difference in the model scale measured wake included in the BEM compared to the simulated wake field in the FVM.

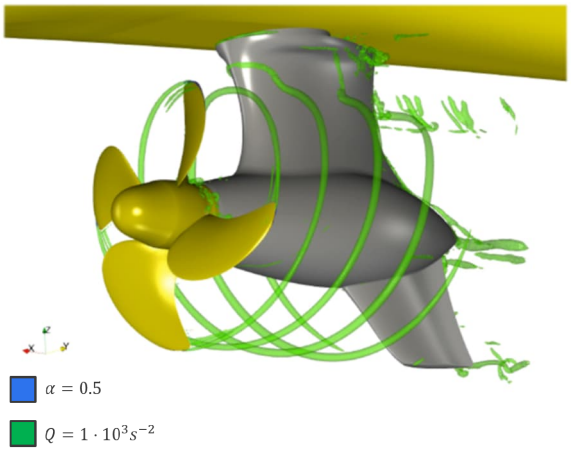

Figure 5: Propeller-housing tip vortex interaction, LES

4.3 Noise Emission

The noise emissions are evaluated based on the transmission path, method and effect location.

4.3.1 Fluid-Structure Interaction

For the unidirectional fluid-structure interaction (FSI) approach, the excitation, as pressure pulses on the unit surface, and the structural response as ERP is given at the first blade passing frequency (BPF) in Figure 6. Highest pressure pulses occur at the locations of interaction between the tip vortex with the unit vertical shaft housing, with an asymmetry depending on the rotation direction of the propeller. The upwards going blade leads to a tip vortex deformation upwards and, as expected, the downwards going blade moves the vortex trajectory down along the shaft housing. A secondary interaction point is the tailfin, in particular on the side facing away from the direction of rotation (left image). Interestingly some minor pressure pulse random noise is visible beginning just beyond the position of maximum thickness of the gondola, shaft and fin profiles. Subfigure 6(b) shows the response of the structure calculated from the ERP for the outer surface nodes of the structure. The dynamic lateral force generated by the propeller leads to a transverse pendulum movement of the housing. The fin has the greatest distance to the pivot point and therefore also the highest oscillation speed, which leads to a maximum of 1.77 mW. Furthermore, there is a slight elevation on the front bearing of the propeller shaft, which is caused by the flow of force from the shaft across the bearing into the housing.

In Figure 7 the first gear mesh frequency (GMF) is split in a similar manner. The very low pressure pulses originate from the hydrodynamic FVM solution, which of course does not naturally show a periodic flow with this frequency. Still identical regions to the first BPF are highlighted as a result of the random frequencies generated by turbulence in the tip vortex and at the separation regions downstream of the position of maximum thickness. The response of the structure is given in Figure 7(b). The contours show two hot spots for the indication of noise. The first one is at the lower bearing of the pinion shaft. It is the result of the local introduction of the bearing force

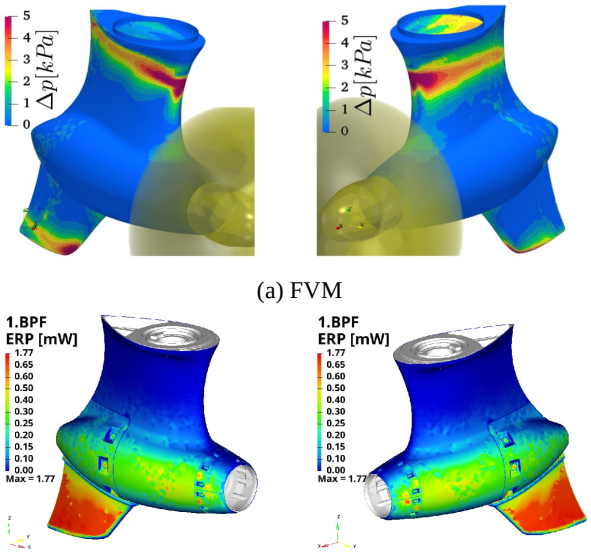

(a) FVM

(b) FEM

Figure 6: Hydrodynamic excitation of thruster housing and structural response at first BPF

into the housing which is caused by the tooth meshing between the pinion and the crown wheel. The second and higher one is in the phased-out area of the shaft. This is caused by a natural frequency and vibration mode of the housing close to the first GMF. Combined these are the main areas that indicate the noise emissions caused by the structure under load at the first BPF and GMF.

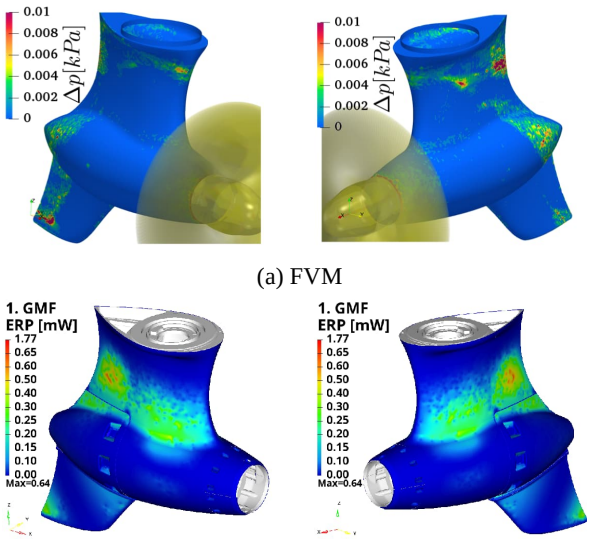

(a) FVM

(b) FEM

Figure 7: Hydrodynamic excitation of thruster housing and structural response at first GMF

4.3.2 Hydrodynamic Interface into the vessel

The pressure pulses introduced into the hull obtained from FVM with active cavitation at the vessel hull surface boundary of the simulation are given in Figure 8 for the first four BPFs. In the first harmonic a maximum of $\Delta p = 0.8kPa$ is reached, which is comparatively low for this vessel type. Resolving the turbulent fluctuations generates an additional $0.1kPa$ directly above the propeller location for the first harmonic, while the higher harmonics lead to more intricate patterns than for RANS turbulence

modelling. At the higher harmonics the fluctuating cavitation pattern at the upwards and downwards rotating blade are visible laterally, which is confirmed by the comparison between the non-cavitating and cavitating case. Note that by switching to the cavitating case there are locations on the hull, that show reduced fluctuations such as between the propeller plane and the vertical unit shaft structure.

These pressure pulses are exciting the vessel structure, leading to vibration in the hull, and induced airborne and underwater noise, possibly over a range of frequencies due to detuning. In addition, this excitation is also affecting the thruster unit foundation and might be reintroduced into the unit along a structural path, however, this transfer path is not included in this investigation.

4.3.3 Emitted Sound

The resulting separate sound emission contributions by the FVM and the FEM are given on a passive sphere with a radius of $r = 3.7m$, which is determined by the minimum radius without intersecting the rotating mesh region. At the first BPF in Figure 9 the FVM produces high pressure pulses in upstream direction with a pattern of minima at the blades passings in (a), while in the downstream direction in (b) the largest contribution is caused by the tip vortex. Again the opposing directions of trajectory deviation by the shaft are highlighted by the vertical shift of the circular pattern. Sound emission resulting from the mechanical vibration in (c) and (d) show a slightly asymmetric radiation with respect to the y-normal plane through the unit. Emission strength is concentrated more lateral in the downstream direction. However, with a maximum of $135dB$ the noise caused by mechanical vibration is much lower than the radiated noise caused by hydrodynamic pulsation with a maximum of $190dB$.

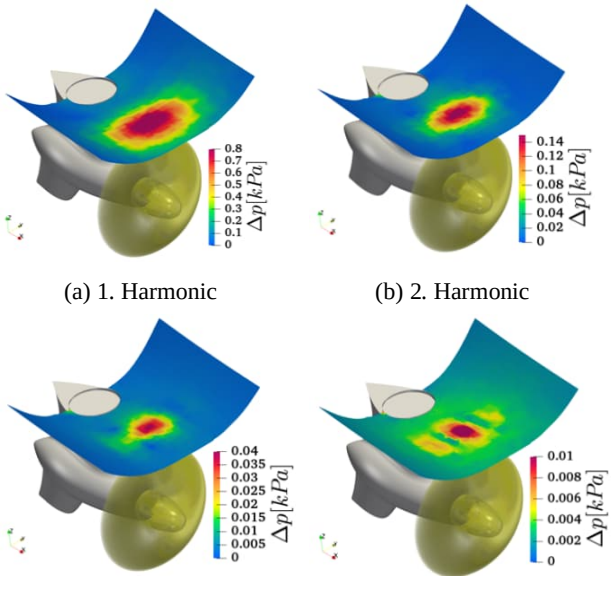

(a) 1. Harmonic (b) 2. Harmonic

(c) 3. Harmonic (d) 4. Harmonic

Figure 8: Thruster hydrodynamic hull pressure, FVM

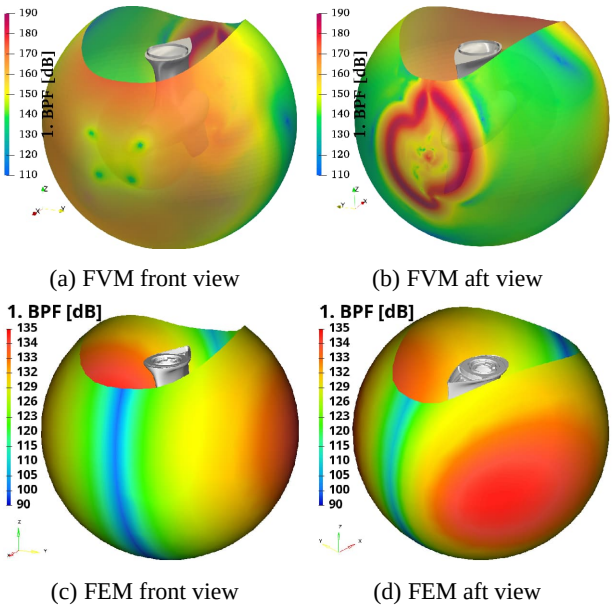

(a) FVM front view (b) FVM aft view

(c) FEM front view (d) FEM aft view

Figure 9: Propeller induced thruster spherical URN emission SPL in vessel wake

Similar to the excitation of the shaft at the first GMF the hydrodynamically caused emissions on this sphere shown in Figure 10 are comparatively low. The emission directivity is dominated by the downstream pattern caused by random nature of turbulence in combination with the tip vortex lifetime at the intersection with the sphere. Although the directivity characteristic is similar between the BPF and GMF for the mechanical emission in (c) and (d), comparing the values yields different results. Here the mechanical noise caused by tooth meshing from the bevel gear dominates. The maximum is around $152dB$, which is much louder than the hydrodynamic noise with $120dB$.

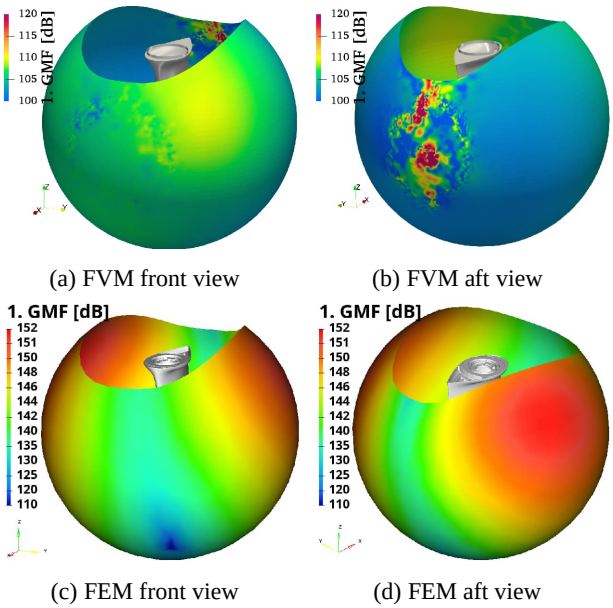

(a) FVM front view (b) FVM aft view

(c) FEM front view (d) FEM aft view

Figure 10: Gear induced thruster spherical URN emission SPL in vessel wake at first GMF

4.3.3 Received Noise

With the BEM, the emission into the fluid domain is modelled by considering the environment around the vessel and the thruster unit. A slice orthogonal to the ship's

x-axis in Figure 11 depicts the sound paths involved in the acoustic pressure field prediction. The propeller is located at the top left corner. The top and the bottom boundaries are the free water surface and the seafloor, respectively. The left boundary is the ship's centerline and the right boundary is located at about five ship lengths $\Delta y = 652m$ away from the ship. For each sound path component the absolute acoustic pressure amplitudes are given on a logarithmic scale at the seventh propeller rotation time step. The sea floor is considered to be at $z = -485m$ according to the measurement. Particularly, the water surface adjacent regions are highly influenced by the sea floor reflection from a comparison between (a), (b) and (d). In addition, the downwards emission direction leads to increased values in the combined result. This highlights the importance of carefully selecting the location of the measuring hydrophones, as due to the resulting patterns extreme values can be detected with respect to the vertical direction.

The received sound pressure level (SPL) for the vessel passing the stationary hydrophone is indicated in Figure 12. The results shown are the measurement in (a) where the CPA is indicated and the FVM results in (b) from domain pressure observers and in (c) from the KFWH method, while (d) shows the FEM. By transforming the time dimension into a geometric one, the horizontal axis between the stationary geometries of the simulations and the mobile vessel with stationary hydrophone may be interchanged in this representation along the x-direction.

While the measurement contains high amplitude broadband emission characteristics from $50Hz$ to $150Hz$, these regions are not captured by the FVM or FEM. Concluding, these broadband contributors may be vessel borne and could possibly be caused by the hull reverberation response to the main generators or alternatively a result of the numerical models predicting insufficient broadband cavitation noise or a combination of both reasons. Both simulations capture the trend of highest noise levels at the CPA and follow similar directivity with larger amplitudes after the vessel passing the measurement point.

The subfigure (b) and (c) are both from the hydrodynamic domain FVM, however, the incompressible hydrodynamic pressure yields more random noise along the frequency dimension and a sharp cut off on this colormap value range at $x = 10m$ downstream of the vessel. The KFWH approach, creates a physical directivity in aft direction of the vessel and leads to more distinct high amplitude frequencies and less random noise. This proves that an acoustic method such as the KFWH is required for observers at a large distance from the source in FVM due to the cell coarsening and subsequently dissipation of high frequency pressure information.

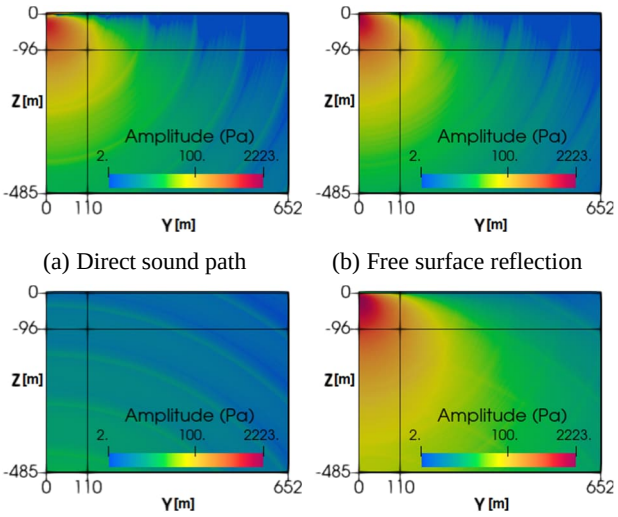

(a) Direct sound path (b) Free surface reflection

(c) Seafloor reflection (d) Sound path superposition

Figure 11: Simulated acoustic pressure field sound paths, BEM

In the same representation of the BEM, FVM and FEM with a focus on the lower frequencies in Figure 13 more details emerge. Added horizontal lines indicate frequencies of importance in the following order beginning from the lowest: shaft rotational frequency, the first four BPFs, the first GMF. A clear correlation with these frequencies in the simulation results is visible along the passing of the vessel.

Figure 14 can be considered as a time-averaged spectrum at the CPA event indicated in Figure 12. A complete SRE unit URN signature in 1/3 octaves at the operation point indicated in Table 2 is labelled FSI and is obtained from the superposition of the FVM and FEM simulation results at the same receiver after correction to source level, which are shown in narrowband representation in the diagram. In the lower frequencies a comparison with the BEM leads to good agreement in trend and value with FSI approach. Comparing with the experimental measurement (Exp-S) in 1/3 octaves, again a good agreement with the simulations is reached except between $60Hz$ and $150Hz$, which agrees with the previous conclusion that it is caused by the vessel and not the SRE unit. Largest deviations between measurement and simulation are around $10dB$ only at distinct frequencies. The experimental data is compared to an identical measurement (Exp-DW) conducted in parallel from an external source (DW-Shipconsult, 2023) and yields excellent agreement confirming the applied measurement approach. It is expected that the environmental conditions of the measurement prevent an accurate representation of the propeller blade frequency peaks below $100Hz$ in narrowband representation. Finally, two limit curves by BV and DNV are provided to achieve a reference of scale of the quietness of the thruster unit.

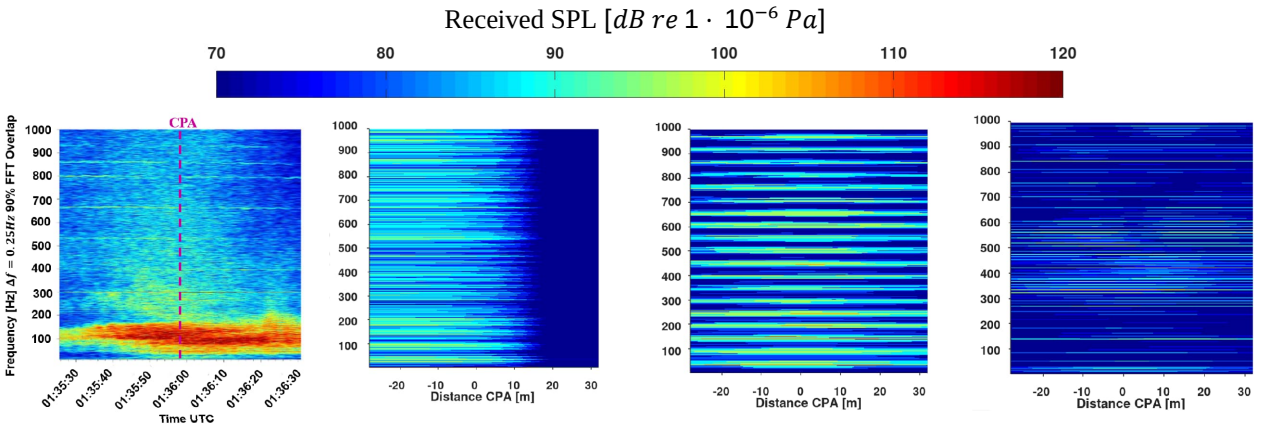

(a) Measured total noise (DW-Shipconsult, 2023)

(b) FVM hydrodynamic pressure

(c) KFWH-method based on FVM hydroacoustic pressure

(d) FEM mechanical noise

Figure 12: Received SPL at the acoustic observer during ship passing

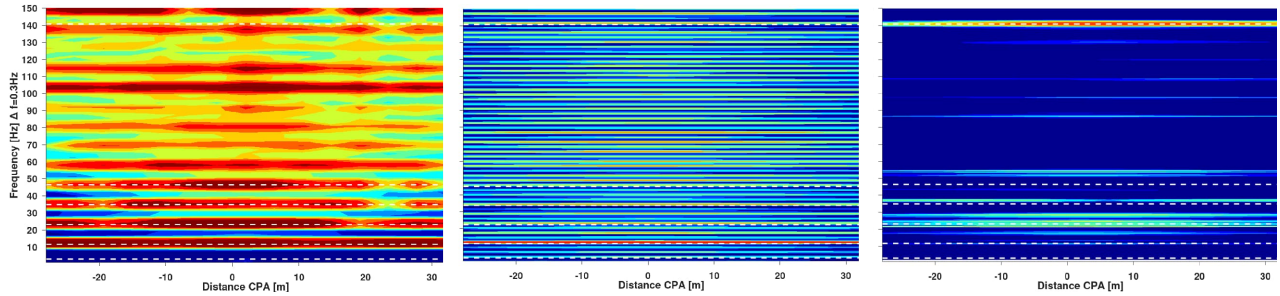

(a) CFD BEM

(b) CFD FVM

(c) FEM

Figure 13: Detail of hydroacoustic pressure $0 < f < 150Hz$ at observer (same colormap as Figure 12)

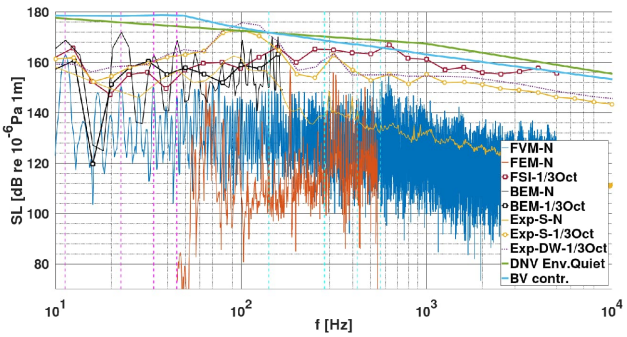

Figure 14: Comparison of measured and simulated radiated noise level

6 CONCLUSION

A SRE 560 type azimuthing pull propeller thruster unit is measured in full scale in a single unit operation test condition and simulated in detail with numerical methods to obtain the complete acoustic emissions onto the hull and into the fluid domain, commonly referred to as URN. BEM and FVM are utilized to evaluate hydrodynamic performance as well as noise emissions and a unidirectional coupling from the FVM to the FEM is applying the excitation of the structure and its acoustic emission, which is combined at the observer. Two independent experiments with very good agreement and the two simulation approaches have moderate agreement, confirming both measurement approach and simulation except between $50Hz$ and $150Hz$, where vessel based contributions may be missing in the simulations.

Although the investigated SRE signature is below URN class limitation curves, it is selected for the measurement based on availability, which in this case is an efficiency optimized unit instead of a noise optimized one. Further noise reductions may be implemented by modifying the tooth geometry of the gears for specific operation points, adjusting the propeller designs to lower efficiency and optimizing the vessel geometry or the operation point for silent operation. Alternatively different gear and engine combinations may be used to shift the frequencies of peaks.

In practice, the structural modes of the unit are highly dependent on the geometry and stiffness of the provided installation, which creates a bidirectional technical interface between unit and vessel that needs to be addressed in future research.

ACKNOWLEDGEMENTS

The authors thank Multi-Maritime for providing the vessel hull geometry, Torghatten Nord AS for the vessel and crew time during measurement and DW-Shipconsult for the measurement data and evaluation. The authors are very grateful for the support and funding by BMWK as project 03SX560A.

REFERENCES

Altair Engineering Inc. (2021). *ALTAIR Optistruct 2021*. Von Radiated Sound Output Analysis: https://2021.help.altair.com/2021/hwsolvers/os/topics/solvers/os/analysis_radiated_sound_output_c.htm#analysis_radiated_sound_output_cabgerufen

Altair Engineering Inc. (2021). *Force:Contact*. Von Altair MotionSolve: https://2021.help.altair.com/2021/hwsolvers/ms/topics/solvers/ms/xml-format_57.htm abgerufen

DW-Shipconsult. (2023). *Underwater Noise Measurements MV Lysoy*. [confidential].

Farassat, F. (1981). Linear Acoustic Formulas for Calculation of Rotating Blade Noise. *AIAA Journal*, 19.9, 1122-1130.

FDS, TUHH. (2023). panMARE: https://www.tuhh.de/panmare/home

Francescantonio, P. (1997). A New Boundary Integral Formulation For The Prediction Of Sound Radiation. *Journal of Sound and Vibration*.

Gaschler, M. (2017). Numerical modelling and simulation of cavitating marine propeller flows. *PhD Thesis*.

Göttsche, U. (2020). *Hamburg University of Technology*, Entwicklung einer numerischen Methode zur Vorhersage der hydroakustischen Schallabstrahlung von Schiffspropellern.

Göttsche, U., Lampe, T., Scharf, M., & Abdel-Maksoud, M. (2019). Evaluation of Underwater Sound Propagation of a Catamaran with Cavitating Propellers. *Sixth International Symposium on Marine Propulsors.* Rome, Italy.

Holm, K., & Schubert, A. (2021). Acoustics in Optistruct. *ALTAIR*. Altair Training Material.

Huang, Y., & Cui, Z. (2020). Acoustic Radiated Power and Radiation Efficiency Calculation with LS_DYNA. *16th International LS-DYNA Users Conference.* Virtual Event.

IMO. (2023). *Revised Guidelines for the reduction of underwater radiated noise from shipping to address adverse impacts on marine life MEPC.1/Circ.906.* International Maritime Organization.

ISO/TC 43/SC 3 Underwater acoustics. (07 2019). ISO 17208-2:2019. International Organization for Standardization.

ITTC. (2017). Underwater Noise from Ships, Full Scale Measurements. *Recommended Procedures and Guidelines*, S. 7.5-04-04-01.

Katz, J., & Plotkin, A. (2001). Low-Speed Aerodynamics. *Cambridge University Press.*

Kimmerl, J., Abdel-Maksoud, M., Nataletti, M., & Savio, L. (2022). Acoustic Comparison of a Ship-Propeller Model in Cavitating Conditions with LES and FWH-Method. *Seventh International Symposium on Marine Propulsors.* Wuxi, China: 7. International Symposium on Marine Propulsors.

Kimmerl, J., Mertes, P., & Abdel-Maksoud, M. (2021). Application of Large Eddy Simulation to Predict Underwater Noise of Marine Propulsors. Part 2: Noise Generation. *Journal of Marine Science and Engineering, 9*, 778.

Kinnas, S., Lee, H., & Young, Y. (2003). Modeling of Unsteady Sheet Cavitation on Marine Propeller Blades. *International Journal of Rotating Machinery*, 9.4.

Krasilnikov, V., Savio, L., Kourosh, K., Felli, M., Abdel-Maksoud, M., Kimmerl, J., . . . Sun, J. (2022). Towards Reliable Prediction of Propeller Noise: Challenges and Findings of the Project ProNoVi. *Seventh International Symposium on Marine Propulsors*. Wuxi, China.

Lidtke, A., Humphrey, V., & Turnock, S. (2016). Feasibility study into a computational approach for marine propeller noise and cavitation modelling. *Ocean Engineering*.

Sezen, S., Atlar, M., & Fitzsimmons, P. (4 2021). Prediction of cavitating propeller underwater radiated noise using RANS & DES-based hybrid method. *Ships and Offshore Structures*.